Can. J. Remote Sensing, Vol. 36, Suppl. 1, pp. S56–S73, 2010

Evaluation of new spaceborne SAR sensors for sea-ice monitoring in the Baltic Sea

Leif E.B. Eriksson, Karin Borenäs, Wolfgang Dierking, Anders Berg, Maurizio Santoro, Per Pemberton, Henrik Lindh, and Bengt Karlson

Abstract. In this study, synthetic aperture radar (SAR) data from the Advanced Land Observing Satellite (ALOS) and the Envisat, RADARSAT-2, and TerraSAR-X satellites were compared to evaluate their usefulness for sea-ice monitoring in the Baltic Sea. Radar signature characteristics at different frequencies, polarizations, and spatial resolutions are presented for three examples from 2009. C-band like-polarization data, which have been used for operational sea-ice mapping since the early 1990s, serve as a reference. Advantages and disadvantages were identified for the different SAR systems and imaging modes. One conclusion is that cross-polarized data improve the discrimination between sea ice and open water. Another observation is that it is easier to identify ice ridges in L-band data than in images from shorter wavelengths. The information content of X- and C-band images is largely equivalent, whereas L-band data provide complementary information. L-band SAR also seems to be less sensitive to wet snow cover on the ice.

Résumé. Dans cette étude, on compare des données RSO (« radar à synthèse d'ouverture ») des satellites ALOS (« Advanced Land Observing Satellite »), Envisat, RADARSAT-2 et TerraSAR-X afin d'évaluer leur utilité pour le suivi de la glace de mer dans la mer Baltique. On présente les caractéristiques des signatures radar à différentes fréquences, polarisations et résolutions spatiales au moyen de trois exemples de 2009. Des données de polarisation semblables aux données en bande C, utilisées dans le contexte de la cartographie opérationnelle de la glace de mer depuis le début des années quatre-vingt-dix, servent de référence. Les avantages et les désavantages des différents systèmes et modes d'acquisition RSO ont été identifiés. Une des conclusions est à l'effet que les données de polarisation croisée améliorent la discrimination entre la glace de mer et l'eau libre. Il a été possible également d'observer qu'il est plus facile d'identifier les crêtes de glace dans les données en bande L qu'à partir d'images à longueurs d'onde plus courtes. Le contenu en information des images en bande X et C est généralement équivalent, alors que les données en bande L fournissent une information complémentaire. Les données RSO en bande L semblent aussi être moins sensibles au couvert de neige mouillée sur la glace.
[Traduit par la Rédaction]

Introduction

Since the early 1990s, spaceborne imaging radar systems have been widely employed for operational sea-ice monitoring and science-driven ice observations. Radar images can be acquired independent of cloud cover and light conditions, which is crucial when frequent updates are required from regions with no or very little sunlight during winter. Spaceborne microwave radiometers, which do not provide as high spatial resolution as imaging radars, are used for wide-coverage sea-ice monitoring in particular for acquiring data on ice extent and concentration over the whole Arctic and Antarctic. Synthetic aperture radar (SAR) is regarded as being optimal for applications requiring high spatial resolution, such as the guidance of ship traffic through ice-infested waters.

With the launch of a number of new satellites it is now possible to combine different SAR imaging modes at three different frequencies (L-, C-, and X-bands). To evaluate the usefulness of data from these new satellites for operational sea-ice services responsible for monitoring the Baltic Sea, the project "Improved sea-ice monitoring for the Baltic Sea" was started in January 2007 (Eriksson et al., 2007; 2010). The project was focussed on sea ice in the northern part of the Baltic Sea, which is an area with a high level of winter traffic. The conditions in the Baltic Sea are special because the water salinity is very low and there is no multiyear ice and no icebergs because of the geographical location.

Received 1 July 2009. Accepted 14 February 2010. Published on the Web at http://pubservices.nrc-cnrc.ca/cjrs on 16 July 2010.

L.E.B. Eriksson[1] **and A. Berg.** Department of Earth and Space Sciences, Chalmers University of Technology, SE-41296 Göteborg, Sweden.

K. Borenäs, P. Pemberton, H. Lindh, and B. Karlson. Swedish Meteorological and Hydrological Institute, Sven Källfelts gata 15, SE-42671 Västra Frölunda, Sweden.

W. Dierking. Alfred Wegener Institute for Polar and Marine Research, Bussestrasse 24, D-27570 Bremerhaven, Germany.

M. Santoro. Gamma Remote Sensing, Worbstrasse 225, CH-3073 Gümligen, Switzerland.

[1]Corresponding author (e-mail: leif.eriksson@chalmers.se).

The main objectives of the project were to (*i*) evaluate how multipolarization L-, C-, and X-band SAR data can improve sea-ice classification and detection of open water areas and ice ridges; and (*ii*) investigate the possibilities of using L-band ScanSAR data as a complement and backup for the C-band ScanSAR data that currently are used for operational sea-ice monitoring. Satellite images were analyzed that cover different ice and weather conditions considered difficult for sea-ice monitoring with single-polarization C-band SAR data. Examples of such conditions are high wind speed over open water and wet snow on top of ice. Field campaigns were organized to coincide with the satellite acquisitions. The objective of this paper is to present results from the evaluation of multipolarization L-, C-, and X-band SAR data for sea-ice classification and detection of open water areas. The possibilities for detection of ice ridges and the operational use of L-band ScanSAR are also discussed, but a quantitative analysis of these topics is left for future publications.

The next section of the paper gives an overview of previous studies and results of sea-ice observations with SAR in the Baltic Sea. The three sections that follow present the satellite dataset, ice conditions, and field data. The results and the discussion and conclusions are presented in the last two sections.

Background

The era of civil spaceborne radar imaging at C-band started with the European Remote Sensing satellite ERS-1 launched in 1991, followed by ERS-2 and the Canadian RADARSAT-1 satellite, both of which have operated since 1995. At present, C-band data can also be obtained from the Envisat and RADARSAT-2 missions. For remote sensing of the polar oceans, C-band is regarded as a reasonable compromise, considering the pros and cons of different frequency bands (Onstott, 1992). The Japanese satellite JERS-1, which acquired data from 1992 to 1998, was equipped with an L-band SAR. However, due to technical problems, the JERS SAR data were only of limited use for sea-ice mapping. Since 2006, L-band images have been available from the SAR onboard the Japanese Advanced Land Observing Satellite (ALOS). The German TerraSAR-X satellite, launched in 2007, and the Italian Constellation of Small Satellites for Mediterranean Basin Observation (COSMO) Skymed constellation, where the first of four satellites was launched in 2007, carry X-band SAR systems. The newer satellite radars can be operated in different imaging modes, i.e., polarization, swath width, spatial resolution, and incidence angle range can be varied. Hence, a promising opportunity is given to investigate the potential of combining images of different frequencies and modes to alleviate ambiguities in separating different sea-ice types and to improve the identification of specific ice structures such as ridges, rafting zones, and narrow leads.

Besides the image data available from the satellite missions mentioned previously, airborne and ground radar measurements were carried out over and on sea ice to assess the performance of different frequency bands for various sea-ice mapping tasks. A general description of various aspects of radar remote sensing of sea ice is provided in Onstott (1992) and, with a focus on the Baltic Sea, in Hallikainen (1992). The benefits and disadvantages of L-band with regard to sea-ice observations are summarized in Dierking and Busche (2006). The most distinct characteristic of L-band in comparison to higher frequencies is the larger radar intensity contrast between deformed and level sea ice. During the melt season, the L-band radar with its greater penetration depth in many cases still provides information about the sea-ice structure underneath a moist snow cover, whereas images from higher frequencies only reflect variations of snow surface properties. A detailed review on the application of X-band radar for sea-ice mapping has not yet been published, but a short summary can be found in Ulander (1991). Further information is provided in Onstott (1992), Gogineni et al. (1992), and Matsuoka et al. (2001; 2002). The X-band radar is more sensitive to the snow and subsurface ice layer. In comparison to lower frequencies, first-year and multiyear level ice and different types of new and young ice can be more easily separated at X-band. The radar intensity contrast between calm open water and sea ice is greater, and X-band is more sensitive to the onset of melt.

Specifically for the Baltic Sea, there are a number of investigations on radar signatures at different frequencies and polarizations that need to be mentioned. In the Bothnian Experiments in Preparation for ERS-1 (BEPERS), airborne SAR images were acquired at X- and C-bands (Leppäranta et al., 1992; Askne et al., 1992). In the initial study, only two ice classes (undeformed ice – open water and deformed ice) could be discriminated in X-band airborne imagery. Using C-band images, it was found that the radar intensity was correlated with the degree of ice deformation. The highest intensities were associated with rubble fields, moderate intensities with rafted ice blocks, and low intensities with smooth level ice (Ulander et al., 1992). In this case, the spatial resolution of the images was 100 m, and the contribution of speckle negligible.

Helicopter-borne scatterometer measurements at C- and X-band indicated that X-band was slightly better suited for sea-ice mapping than C-band (Hyppä and Hallikainen, 1992). At like-polarization (HH, VV), only ice ridges could be clearly recognized in the data, whereas the radar intensities for thick level ice overlapped with those of hummocked ice, new ice, and open water. At cross-polarization (HV, VH), a sufficient discrimination was possible between three groups, namely new ice – open water, thick level ice, and hummocks – ice ridges. It was concluded that the parallel use of like- and cross-polarized channels improved the discrimination of ice types significantly. Although the dataset used for the study presented in Hyppä and Hallikainen (1992) was rather limited, a more compre-

hensive analysis including scatterometer data from various campaigns carried out between 1992 and 1997 was described in Mäkynen and Hallikainen (2004). Most data were acquired at times when the snow was moist or wet. The radar intensity distributions of eight different ice cover classes were investigated (open water leads, nilas, smooth and rough level ice, slightly and highly deformed ice, loose and frozen brash ice). It was found that it was not possible to distinguish ice classes reliably from one another in an automated procedure using only the radar intensity as a criterion. The best results for separating deformed ice, level ice (including slightly deformed ice), and nilas were achieved at C-band at an angle of 45°, including also the standard deviation of the measured intensity values for each ice class. However, the classification performance was almost similar at X-band.

By comparing ERS-1 and helicopter-borne optical images for three campaigns, Dammert et al. (1994) concluded that it was possible to discriminate up to seven ice classes visually when data were collected under dry and cold conditions, but only three under warm and wet conditions. Using radar intensity and image texture (which is related to the standard deviation of the intensity) as classification criteria, and combining the different datasets, only three classes (dry snow) and two classes (wet snow) could be reliably distinguished. It was observed that radar signatures of the ice classes changed slightly from season to season, which may be caused by variable environmental conditions during ice formation.

Measurements of radar signatures of Baltic Sea ice at L-, S-, C-, and X-bands were carried out by means of a ship-based scatterometer (Dierking et al., 1999). Data could only be acquired over level ice, so any conclusions about the classification performance of the different frequency bands were not possible. The analysis of the data in combination with scatter modeling show that the backscattering responses at X-band can be dominated both by air bubbles in the uppermost part of the ice volume and by the roughness of the snow–ice interface. The volume contribution depends on air bubble size and fraction and on the radar incidence angle. At C- and S-bands, the roughness of the snow–ice interface dominates the magnitude of the backscattered intensity. At L-band, strong scattering contributions arising from the ice–water interface were also observed in some cases. These observations are in line with the fact that the radar responses at the different frequencies are influenced by the penetration depth in the ice (as a function of ice salinity and temperature) and by the sizes of scattering elements (air bubbles, brine cells, surface undulations) relative to the radar wavelength. In Baltic Sea ice, penetration depths may vary from more than 0.7 m at L-band and a salinity of 0.5 to only a few centimetres at X-band and a salinity of 4.0 (theoretical estimates).

The utilization of polarimetric SAR at C- and L-bands for sea-ice classification was investigated in a number of studies on the basis of airborne data acquisitions. It was observed that the intensity range covered by the different ice types was larger at L-band than at C-band. It was easier to separate deformed and level ice in L-band intensity images (Dierking and Askne, 1999; Dierking et al., 1997). For this purpose, images of the phase difference between VV and HH polarization could be used at L-band and of the copolarization ratio VV:HH at C-band (Similä et al., 1998). A classification scheme was developed for C- and L-band imagery, separating thin ice, smooth level ice, rough level ice, and ridges – brash ice (Skriver et al., 2004). It was found that the overall classification accuracy was larger at L-band (95%) than at C-band (87%). A comprehensive summary of the microwave signature of Baltic Sea ice can be found in Mäkynen (2007) and on modeling Baltic Sea ice backscattering in Carlström (1995).

Satellite images

The SAR data used in this paper are listed in **Table 1.** Data from the ALOS phased array type L-band SAR (PALSAR) were obtained in fine-beam single-polarization (FBS) mode, with HH polarization and a look angle of 34.3°, in fully polarimetric (PLR) mode with a look angle of 21.5°, and as ScanSAR wide-beam data (WB) at HH polarization. Data from the Envisat advanced SAR (ASAR) were used in wide-swath mode (WS) and in the high-resolution alternating polarization mode (AP). For the TerraSAR-X, strip-map dual-polarization mode (SM) data and ScanSAR images (SC) were ordered. In terms of spatial coverage and resolution, TerraSAR-X SC corresponds to PALSAR FBS and ASAR AP modes. RADARSAT-2 data in the dual-polarization (HH, HV) ScanSAR Wide (SCW) and ScanSAR Narrow (SCN) modes were also available for the evaluation, as well as data in the quad-polarization fine-resolution (FQ) mode. Details about the selected observation modes are given in **Table 2**.

All SAR images were obtained in radar geometry, i.e., in range–azimuth coordinates, except the TerraSAR-X SC and PALSAR WB images from April that were delivered as geocoded ellipsoid corrected (GEC). Multilook processing was applied to reduce speckle noise. The multilook factors were determined based on the initial pixel size of the data and the desired output spatial resolution. More details are provided in the Results section. In most cases data were obtained in a form that only required application of a calibration constant to obtain calibrated sigma zero (backscattering coefficient, σ^0) images. The calibration constants are given by the processing facilities. To allow intercomparison between datasets, the images were geocoded to the Swedish coordinate system RT90. Image geocoding was carried out using a look-up table that described the relationship between the radar and the map geometry (Wegmüller, 1999). The transformation described in the look-up table is set up based on orbital data. In case of inaccuracies of the orbital data, refinement of the look-up table is necessary. This is implemented in the form of a cross-correlation algorithm between the SAR image and a reference image for the output geometry. Matching features in the two images are used to detect possible offsets, which

Table 1. List of SAR images used in this paper, acquisition dates and times, and meteorological observations from nearby weather stations.

Date (year–month–day)	Satellite and observation mode[a]	Acquisition time (UTC)	Temp. (°C)	Wind speed (m/s)
2009–02–19	ALOS PALSAR FBS	2032	−16	0
2009–02–19	Envisat ASAR WS	1941	−16 to −15	0–5
2009–02–20	TerraSAR-X SM	0521	−17 to −15	0–3
2009–02–20	Envisat ASAR WS	0920	−19 to −10	3–4
2009–03–21	TerraSAR-X SM	1546	+1	6
2009–03–21	RADARSAT-2 FQ	1543	+1	6
2009–03–21	Envisat ASAR WS	0909	0 to +4	2–9
2009–03–22	ALOS PALSAR PLR	2013	−5 to −4	1–4
2009–03–22	RADARSAT-2 FQ	0523	−8 to −7	0–6
2009–03–22	Envisat ASAR WS	2007	−7 to −4	0–4
2009–04–23	ALOS PALSAR WB	0924	+9	5
2009–04–23	TerraSAR-X SC	1546	+2	5
2009–04–23	RADARSAT-2 SCW	1623	+1 to +9	4–6
2009–04–23	Envisat ASAR WS	2001	0 to +2	3–5
2009–04–24	RADARSAT-2 SCN	1552	+2 to +8	3–7

[a]AP, alternating polarization; FBS, fine-beam single polarization HH; FQ, fine-beam quad polarization; PLR, polarimetric (quad polarization); SC, ScanSAR; SCN, ScanSAR narrow; SCW, ScanSAR wide; SM, strip map; WB, wide beam; WS, wide swath.

are directly related to errors in the geocoding transformation. Because the image primarily covered water surfaces and rather flat coastal zones, offsets were estimated manually in case the cross-correlation algorithm did not find a sufficient number of matching features. Comparison of geocoded images showed an agreement at the subpixel level.

Ice conditions in the Baltic Sea

The ice in the Baltic Sea is annual, with ice formation starting in November in the coastal areas of the northernmost parts of the Bothnian Bay. The ice cover then moves southward and outward from the coast. The more shallow area between the Bothnian Bay and Bothnian Sea (the Quark) freezes before the central part of the Bothnian Bay is ice covered. The maximum ice extent for the period 1961–1990, based on all available ice charts for the period, is estimated to be approximately 150 000 km^2 (L. Axell, personal communication), but the interannual variability is large (Seinä and Palosuo, 1996). In spring, the ice starts to melt from the south, and the ice is generally completely gone by the end of May.

The weather conditions during the period 2007–2009 were mild, with maximum ice extent below the climate mean.

Table 2. Properties and acronyms for the selected observation modes.

		Property				
Imaging mode	Acronym	Swath width (km)	Spatial resolution (m)	Polarization	Incidence angle (°)	Noise-equivalent σ^0 (dB)
ALOS PALSAR, fine beam, single polarization	FBS	70	9–10 (ground range)	HH	36.6–40.8	−29 to −24
ALOS PALSAR, polarimetric mode	PLR	30	29–31 (ground range)	VV + VH + HH + HV	22.8–25.2	−31 to −30
ALOS PALSAR, wide beam 1	WB	361	71–157 (ground range)	HH	18.0–43.0	−32 to −23
Envisat ASAR, wide swath, medium resolution	WS	400	150 (ground range)	HH	19–43	−20.8 to −26.2
RADARSAT-2 fine beam, quad polarization	FQ	25	5.4 (slant range)	VV + VH + HH + HV	20–41	
RADARSAT-2, ScanSAR narrow, dual polarization	SCN	300	37.7–79.9 (ground range)	HH + HV	20–46	
RADARSAT-2, ScanSAR wide, dual polarization	SCW	500	72.1–160.0	HH + HV	20–49	
TerraSAR-X strip map, dual polarization	SM	15	6.6–7.7 (ground range)	HH + HV or VV + HH	20–45	−19
TerraSAR-X ScanSAR	SC	100	17.6–19.2 (ground range)	HH	20–45	

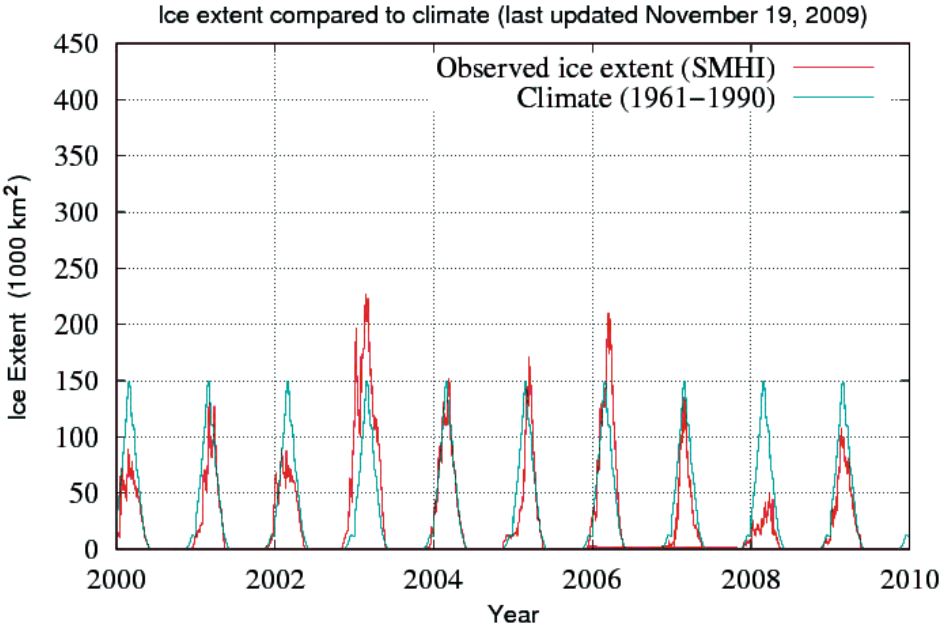

Figure 1. Observed ice extent in the Baltic Sea for the years 2002–2009 and climate mean ice extent for the period 1961–1990. The graph was created by L. Axell (Swedish Meteorological and Hydrological Institute).

This is demonstrated in **Figure 1**, which shows the ice extent for the winters 2002–2009. For the 2007–2008 ice season, the value for the maximum ice extent was the lowest found in the ice records for the last 100 years (Grafström and Kilgren, 2008). The satellite images considered in the present study are from the 2008–2009 ice season, which started with a slow freezeup. Rapid growth of ice took place in February, and the maximum ice extent was reached already on 20 February. The ice season was over at the end of May.

The salinity in the Baltic Sea is very low and decreases towards the north. The values in the Bothnian Bay, the northernmost part of the Baltic Sea, are in general 3.0 at the surface and 4.0 at greater water depths. Near the river outlets the surface values are close to zero. Standard salinity for open ocean is 35. The salinity of the Baltic Sea ice has been measured during several field campaigns, e.g., Granskog et al. (2006) reported typical salinity values for the Bothnian Bay in the interval 0–0.6. This can be compared with the conditions in the Arctic, where first-year ice has a mean salinity of 2.0–8.0 (Vancoppenolle et al., 2009). During the BEPERS-88 expedition in the southern part of the Bothnian Bay, the mean ice salinity was found to vary between 0.5 and 1.0 along vertical profiles, whereas the mean brine volume varied between 1% and 4%, the former value pertaining to the uppermost 20 cm of the ice (Fransson et al., 1990). According to Leppeäranta and Manninen (1988), the temperature must be at least −1 °C if the bulk ice salinity is 1.0 for the Baltic Sea ice to become permeable (presuming that the relation between ice porosity and permeability found for ice in saline waters is also valid for the brackish Baltic Sea ice).

Field data

To validate the information retrieved from the satellite images, it was essential to acquire additional optical data with sufficient spatial coverage. This was mainly achieved by taking photographs during helicopter flights. Photographs were taken every 10 s with a Nikon D700 camera, and each image covered an area equal to 1000 m × 1500 m on the ground for the standard flight altitude of 600 m. The airborne observations were complemented with ice and snow measurements on the ground. These were mainly carried out during the flights, with the helicopter landing on the ice. Typically, in situ ice data could be obtained for one or two spots along the flown profiles. The type and number of observations on the ice depended on the prevailing conditions. The sea-ice thickness, snow thickness, and snow density were determined at a number of sites on the level ice. The ice thickness was measured using a manual ice drill with a diameter of 13 cm, and the snow density was determined by weighing snow samples of standard volume from the upper 5 cm of the snow cover. Ice cores, 9 cm in diameter, were obtained from an ice-core drill, and the uppermost part was cut in 2 cm thick slices and photographed for air bubble detection (**Figure 2**). Observations of air and snow temperature were made and notes were taken on the ice structure. The snow temperature was measured with a thermal probe approximately 2 cm from the surface and at several points. Standard meteorological observations (wind, temperature, and relative humidity) were available from the following stations along the Swedish coast: Järnäsklubb (63.44°N, 19.68°E), Holmön (63.81°N, 20.87°E), Bjurök-

Figure 2. Slice from an ice core (diameter 9 cm) showing a large number of air bubbles. Photograph taken on 22 March 2009.

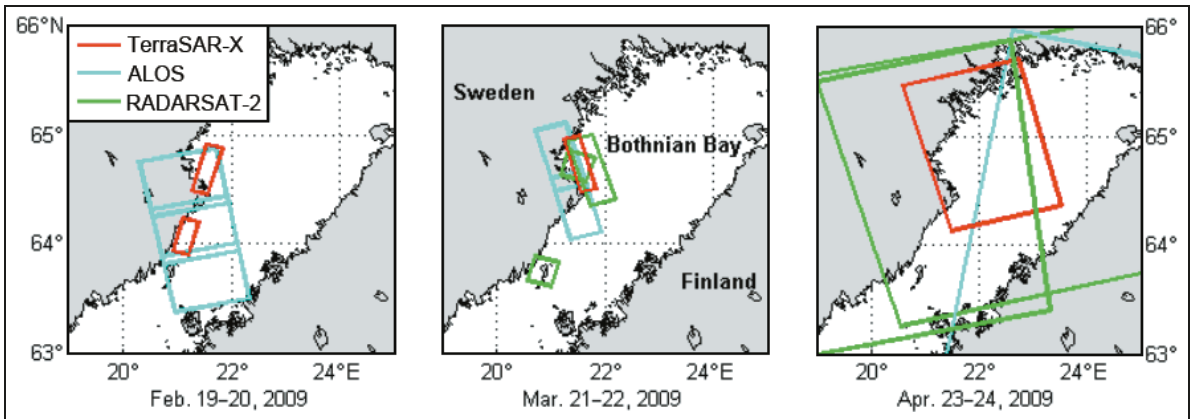

Figure 3. Maps showing the geographic extent and location of the satellite images used in the examples. For all dates except 24 April 2009, there also exist Envisat WS images. These have not been included because they are large enough to cover the entire area of interest.

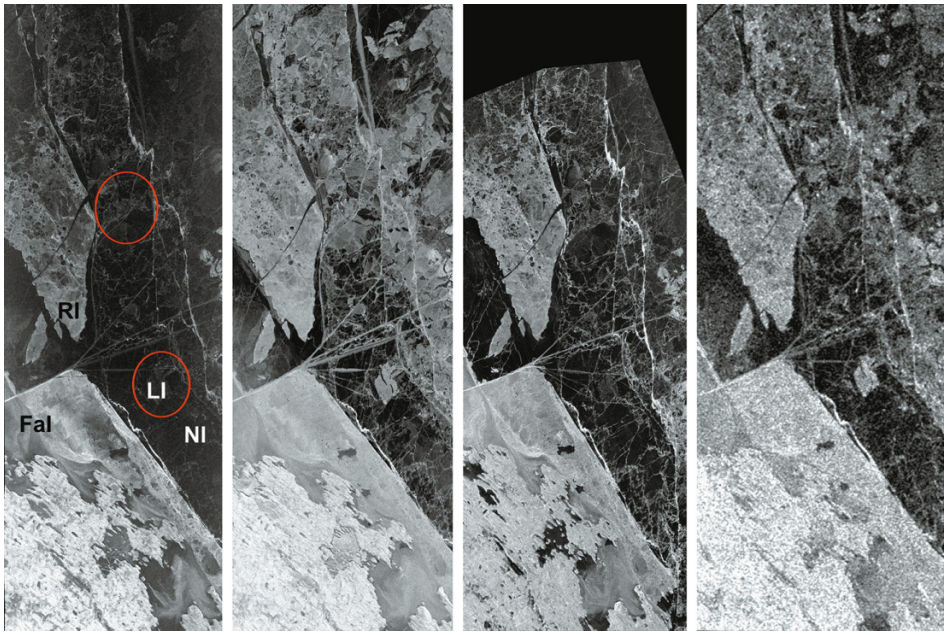

Figure 4. Sea ice observed at different frequencies. From left to right: TerraSAR-X, HV polarization; TerraSAR-X, HH polarization; PALSAR, HH polarization; and ASAR, HH polarization. The red ellipses indicate level ice (LI) characterized by backscattering coefficients that are sensitive to frequency and polarization. FaI, fast ice; NI, new ice; RI, rough ice.

lubb (64.48°N, 21.58°E), Pite-Rönnskär (65.03°N, 21.57°E), and Rödkallen (65.31°N, 22.38°E). A map of the area is shown in **Figure 3**.

Results

This section presents results that illustrate the pros and cons of the different frequencies and imaging modes. The selection of dates was based on the availability of satellite imagery and additional helicopter and field data. Data products acquired at X-, C-, and L-bands were available in 2008 and 2009, but only in 2009 were data from all three frequencies available within a time period short enough to allow a comparison. For this reason, all presented results are from 2009. **Table 1** lists the SAR image acquisition times and the corresponding air temperature and wind speed observations from nearby weather stations. The locations and geographical extents for the satellite images available at these occasions are shown in **Figure 3**.

In the following, we focus in particular on frequency and polarization. Because of the sea-ice drift, it is necessary to combine data for a given area with a sufficiently short time between the acquisitions. Considering also data acquisition plans and priorities for each satellite, the images that are available for comparison usually differ in more than one radar parameter (frequency, polarization, incidence angle, spatial resolution, noise level), which has to be taken into account in the analyses.

Results from 19 and 20 February 2009

Data were acquired on 19 and 20 February 2009 from TerraSAR-X, ALOS PALSAR, and Envisat ASAR close to the Swedish coast between 64 and 65°N. On both days, photographs were taken on helicopter flights over the coastal fast-ice belt. The sky was mostly overcast during the flights, so the intensity contrasts in the visual photographs are relatively low and details of the ice structure (in particular regarding the surface roughness) are difficult to recognize.

The TerraSAR-X data were acquired in dual-polarization SM mode at HH and HV polarization. The pixel size of the images used for the analysis is 20 m × 20 m, and the incidence angle range is from 20.0 to 21.8°. From the PALSAR FBS image, a section was used with an incidence angle range from 38.8 to 40.8° and a pixel size of 20 m × 20 m. For the ASAR WS, a section was used with incidence angles ranging from 21.2 to 25.1° and a pixel size of 75 m × 75 m. The PALSAR and ASAR images were acquired at HH polarization. The effective number of looks is >15 in all cases. In **Figure 4**, the overlap region of all three images is shown and is smaller than the total sizes of the respective images. The visual information content is very similar in all images, with variations at local scale. Clear differences are seen, for example, between the HV- and HH-polarized images at X-band (TerraSAR-X). In these images, level ice areas, marked by red ellipses, are observed for which the radar return is relatively high at like polarization but low at cross-polarization. All in all, the TerraSAR-X image

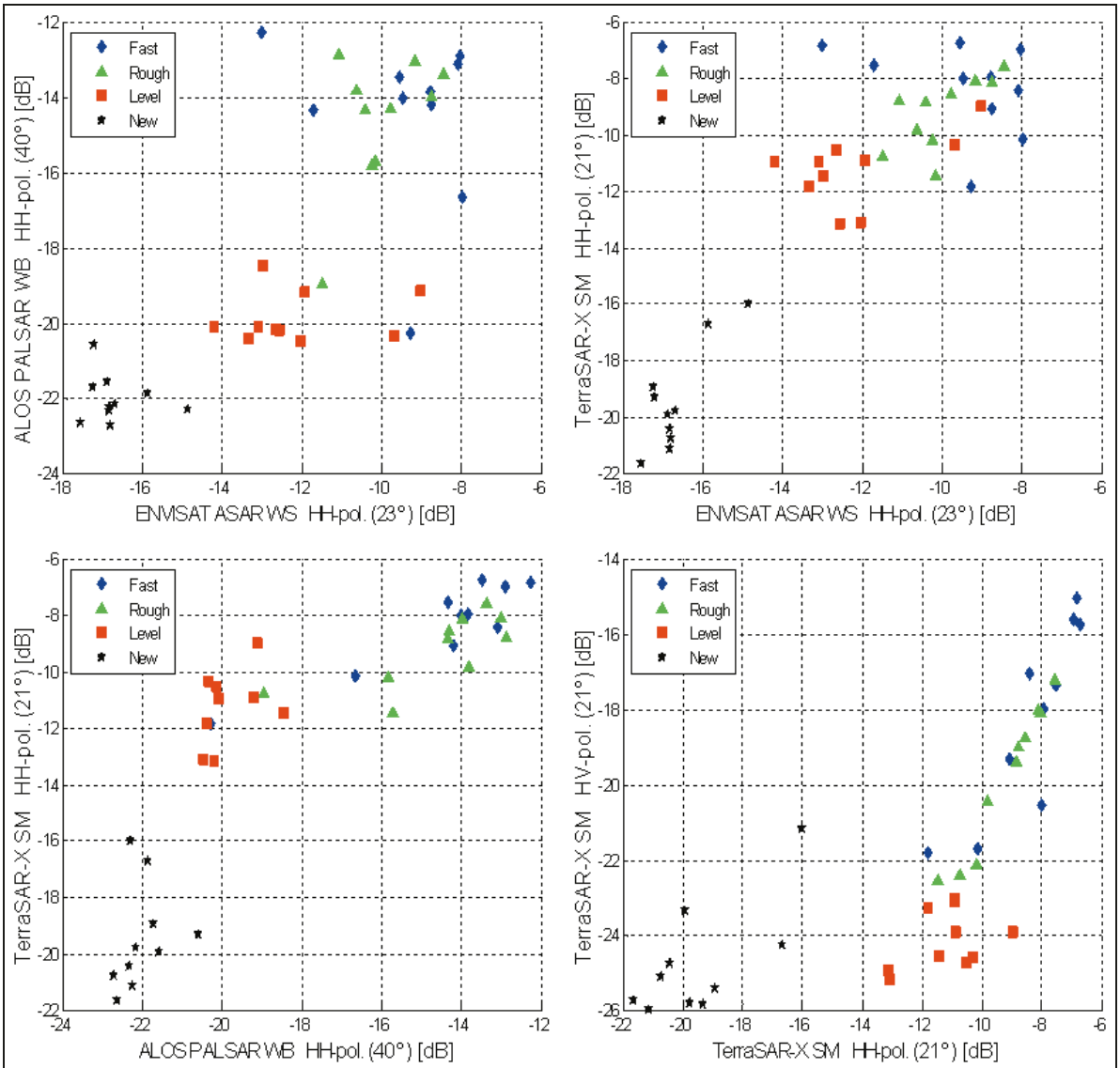

Figure 5. Backscattering coefficients of the major ice classes observed on 19 and 20 February 2009 at the test site in the Baltic Sea.

acquired at HV polarization reveals a greater correspondence with the PALSAR L-band image, whereas at like polarization the X-band resembles the ASAR C-band image (see also **Figure 5**, in which clusters of backscattering coefficients are shown for different ice classes). However, when choosing image products, the generally much lower signal-to-noise ratio at cross-polarization has to be taken into account. Deformation structures such as ridges and rafting zones are easier to recognize in the PALSAR image than at TerraSAR-X cross-polarization. Also, most structures stand out clearly at X-band like polarization, although the intensity contrast relative to the surrounding level ice is often lower than that at L band. Here, the very good spatial resolution of the TerraSAR-X contributes significantly to the perceptibility of narrow linear ridges and rafting patterns. In the ASAR WSM image with an effective spatial resolution of about 150 m, only coarser patterns can be recognized, consisting of ridge clusters.

By comparing the high-resolution TerraSAR-X (HH polarization) and the coarse-resolution ASAR images it can be concluded that an experienced sea-ice analyst can easily visually retrieve the most relevant information on sea-ice conditions from wide-swath data products.

For a quantitative analysis, regions of interest (ROIs) were placed over the images, grouped according to different ice classes indicated in **Figure 4**. Since ROIs of 8 × 8 pixels (ASAR) and 30 × 30 pixels (TerraSAR-X, PALSAR) in size were used for extracting the magnitudes of the backscattering coefficient, the influence of speckle on the results is negligible. The ice classes are fast ice (FaI in **Figure 4**, attached to the coast and appearing bright in all images), new ice (NI, dark in all images, with indications of

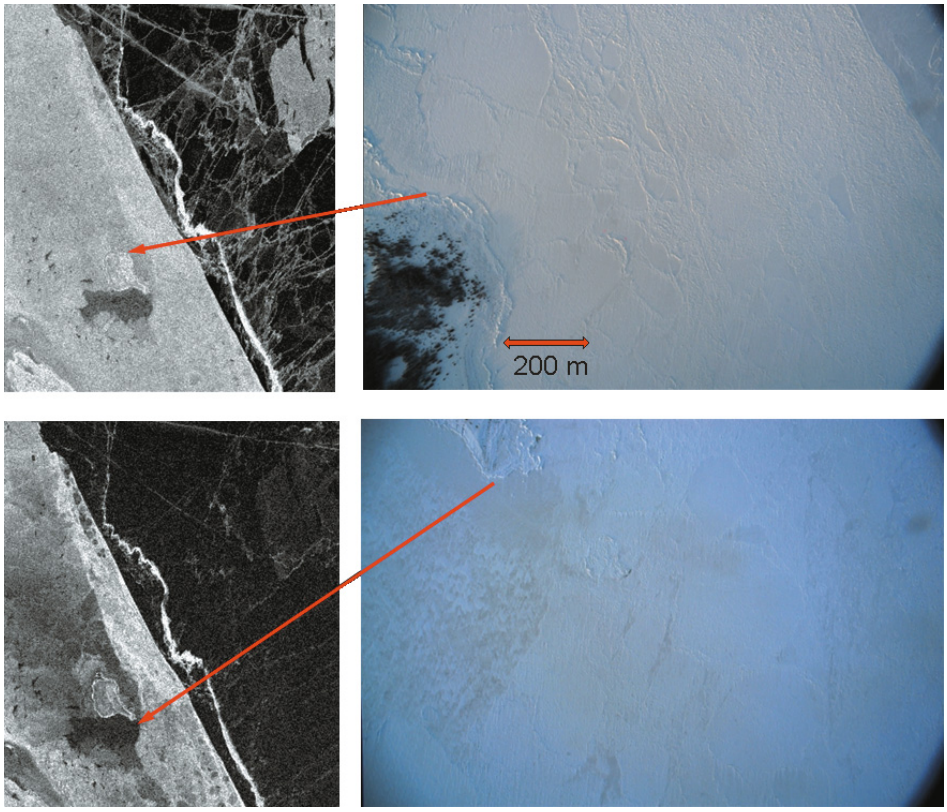

Figure 6. TerraSAR-X HH polarization (left column, upper image) and HV polarization (left column, lower image). Right column: photos taken during helicopter flights. All images are from 20 February 2009.

rafting and ridging), and ice floes with varying degrees of surface roughness (rough ice RI and level ice LI). The RI class reveals characteristics of backscattering that can be described by the geometrical optics approach. The backscattered signal is proportional to the occurrence probability of surface patches, which reflect the incident radar wave specularly into the direction of observation (e.g., Dierking, 1999). One condition is that the reflecting surface elements need to be larger than the radar wavelength. If level ice appears bright over the frequency range from X- to L-band, it is broken, with single ice fragments larger than 30 cm shifted upwards and resting in a tilted position (hummocked ice). Such ice conditions were also frequently observed during a cruise with the research vessel RV *Aranda* in March 2009 in the region over which our satellite data were acquired. Class LI, on the other hand, shows a decrease in the backscattered radar intensity from higher to lower radar frequencies. This behavior is typical for smoother level ice surfaces (LI).

Backscattering coefficients are shown in **Figure 5**. The incidence angles at which the ASAR and TerraSAR-X data were taken are in the range of 21–23° (comparable to the angle interval covered by ERS-1 and ERS-2), and the incidence angle for the PALSAR data is 40°. For incidence angles between 30 and 60°, a considerable sensitivity of the intensity contrast between level and deformed ice was not recognized (Dierking and Dall, 2007). In general, however, ridges are more difficult to distinguish from the surrounding level ice at lower incidence angles (e.g., Melling, 1998; Pearson et al., 1980). It can be concluded from **Figure 5** that level and new ice are difficult to separate in the TerraSAR-X HV-polarization images, but deformed and fast ice can be separated from new and level ice. At X-band HH polarization, new ice forms a distinct cluster, but the other three ice types reveal a considerable overlap. The backscattering coefficients of deformed and fast ice overlap completely in all images.

The air temperature was well below 0 °C on 19 and 20 February, and thus both volume- and surface-scattering contributions must be considered in the interpretation of the radar signatures. Information regarding the volume structure of land-fast ice is only marginal, but a photograph of the uncovered ice surface indicates that air bubbles were present in the ice bulk. The backscattered cross-polarized intensity from the ice surface is usually relatively low but can be higher for contributions from the volume (e.g., Thomsen, 2001). Hence, the X-band image at HV polarization indicates that in fact a considerable volume contribution can be assumed for a number of locations on land-fast ice. This is also valid at C-band, since the wavelength

difference between X-band and C-band is only small. In the case of C-band, the balance between volume scattering and surface scattering is slightly more towards the latter. The effect of changing surface characteristics on the backscattered radar signal is clearly visible in the examples shown in **Figure 6**.

In summary, the following conclusions are drawn from this example. The influence of microscale features (millimetre- to centimeter-scale surface roughness, air bubbles) is large enough for significant intensity changes at X- and C-band like polarization. From other studies it is known that the polarization difference between HH and VV polarization is also affected by the microscale surface roughness (e.g., Bragg scattering) (Dierking et al., EMAC-Report, 1997). Such characteristics have only a minor influence at L-band. The cross-polarization signal increases with an increase in the deviation of the air bubble shape from a sphere, and it depends on the degree of their alignment (Nghiem et al., 1990; 1995). Ice areas appearing bright at both shorter and longer wavelengths are characterized by large-scale deformations on the decimetre to metre scale (broken ice, hummocks, ridge clusters, brash ice). Large-scale deformation features change the effective ice thickness, e.g., rafting doubles the ice thickness locally, and ridges may increase the average thickness in a given area significantly. Hence, signature variations at L-band, which is less sensitive to the influence of microscale structures such as millimetre–centimetre surface roughness and air bubbles, may reveal a higher correlation with the effective ice thickness changes. The example of **Figure 4** shows also that the large-scale ice situation (scale of kilometres) can be easily recognized in the ASAR wide-swath mode images by an experienced sea-ice analyst, demonstrating that high-resolution images at all frequencies provide additional "fix points" to improve the robustness of visual classification. The information contents of X- and C-band images are to a high degree equivalent, whereas L-band data provide complementary information because they are considerably less affected by microscale ice structures.

Results from 21 and 22 March 2009

Multipolarization data were acquired on 21 and 22 March 2009 over the northwestern part of the study area by ALOS (PLR), RADARSAT-2 (FQ), and TerraSAR-X (SM HH–HV) (see **Figure 3**). In addition, an Envisat WS image in HH polarization was available for both days. To minimize duplication, results are reported for the image from 21 March. Due to wind blowing towards the northeast at the time before the acquisitions, large parts of the overlap area for the satellite images were ice free, with fast ice along the coast and a large patch of drifting ice in the east. Wind speeds and temperatures as observed by meteorological stations along the Swedish coast are indicated in **Table 1**.

Figure 7 shows two sections (A and B) of the overlap area as it appears in L-, C-, and X-bands in copolarization and cross-polarization (HH and HV, respectively). The ALOS PALSAR images have a pixel size of 50 m × 50 m (28 looks), and the selected sections cover incidence angles of 24–25°. The pixel size for the RADARSAT-2 images is 30 m × 30 m (18 looks), and the covered incidence angles range from 20 to 21°. For Envisat ASAR and TerraSAR-X, the corresponding pixel sizes are 75 m × 75 m (21 looks) and 20 m × 20 m (64 looks), respectively, and the incidence angles are around 33° for ASAR and 21–22° for TerraSAR-X. For the quantitative analysis, ROIs with sizes of about 600 m × 600 m were selected for four ice types and for open water. Ten ROIs were selected for each ice type, and the sigma naught values were registered.

The first section (A) of **Figure 7** covers the fast ice, and the second section (B) the drifting ice. From west to east, the images in section A contain land, in the form of a few scattered islands, rough deformed fast ice, level fast ice, and open water. The transition zones between these land–ice–water types have been marked with three red ellipses in one of the PALSAR images. As can be seen in the area marked by the leftmost red ellipse, the backscatter for the deformed sea ice is in many cases as high as that for land in the HH-polarized images, whereas in the HV images the border is clearly visible, especially at L-band, where the backscatter for land is significantly higher.

The helicopter landed on the border between the deformed and level fast ice, and ice cores showed that the deformed ice was about 1 m thick and the level ice about 30 cm thick. The photographs in **Figure 8** illustrate the difference in roughness and snow cover. The surface of the deformed ice is made up of broken pieces of ice, refrozen cracks, and piles of snow, partly with crust. The level part consists of relatively clear ice with a lot of air bubbles in the top layer (see **Figure 2**) and patches with a thin, dry snow cover. The days before the image acquisitions had been warm, with temperatures well above the freezing point. The unusually smooth and highly reflecting parts of the ice indicate that the snow on the ice, and maybe even the top layer of the ice, had melted and the water layer had then frozen when the temperatures dropped during the night. The border between the smooth and deformed ice types is clearly visible in all frequencies, in both HH and HV polarization and in both high and low (ASAR WS) resolution. This is explained by the fact that the surface roughness and structure of the two ice types are significantly different for all wavelengths. For the shorter wavelengths, the differences in snow accumulation might also influence the backscatter. The level ice looks less homogeneous in L-band HV than in the other images.

The rightmost red ellipse in **Figure 7** is located at the border between the level ice and open water. The copolarized backscatter from water is highly variable and related to the wind speed and direction. As can be seen in **Table 1**, the RADARSAT-2 and TerraSAR-X images were taken only 3 min apart, so the wind conditions should be comparable. In this case, with a wind speed of 6 m/s, the backscatter from the water is as high as that from the

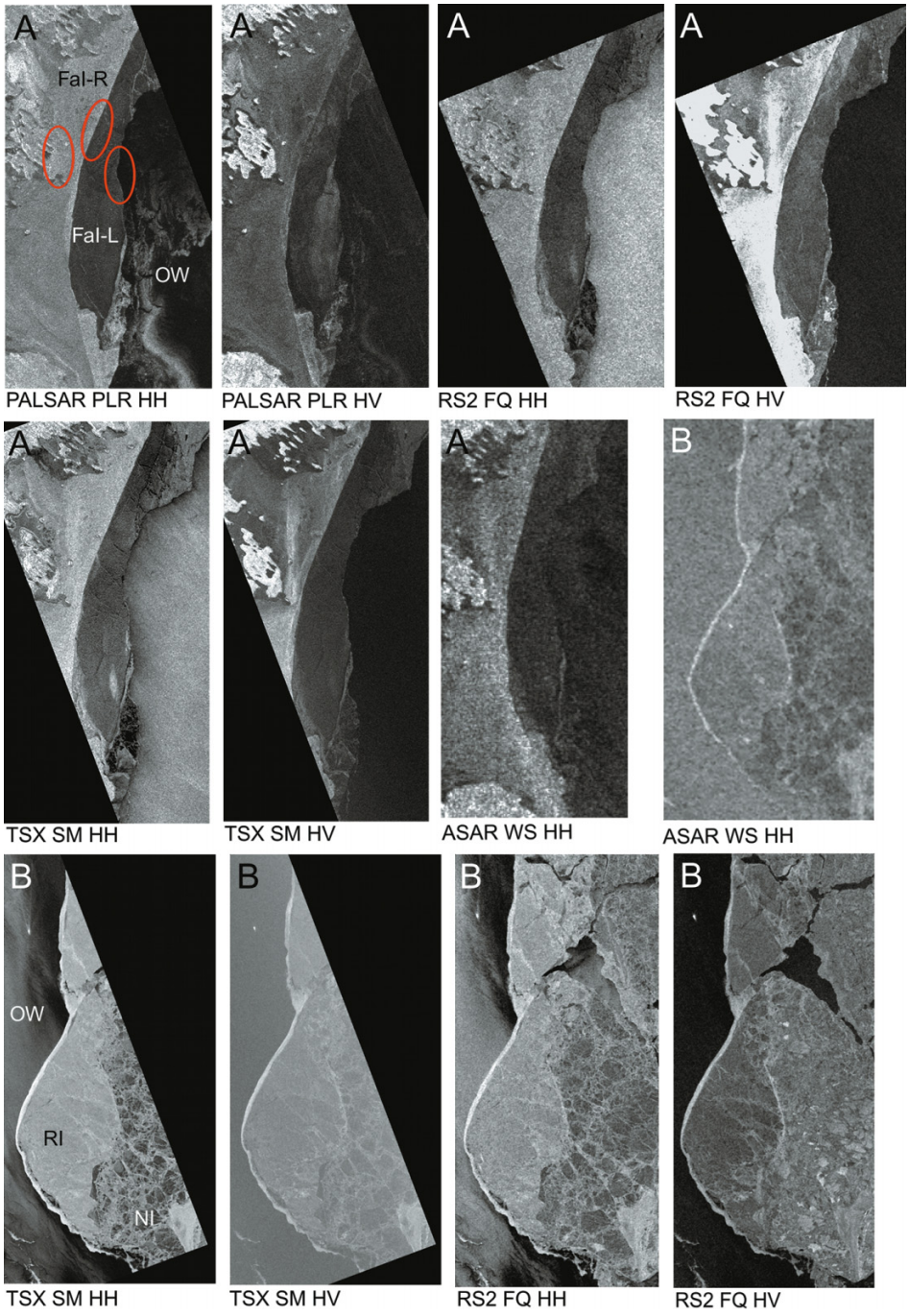

Figure 7. Sections of satellite images covering the ice types discussed in the text. Rough fast ice (FaI-R) and level fast ice (FaI-L) are indicated in section A, and rough ice (RI) and new ice (NI) in section B. Open water (OW) is present in both sections. The PALSAR images are from 22 March 2009, and all others are from 21 March 2009. The acquisition time for each satellite image is listed in **Table 1**.

deformed ice, and the level fast ice has a lower backscatter. It is easy to imagine wind conditions when it is not possible to differentiate between open water and level ice. The ASAR WS image gives an indication of such a case. In the HV polarization the backscatter from water is generally significantly lower than that from land and most of the ice types and thereby provides a more robust separation of ice and water.

Section B in **Figure 7** contains, from west to east, open water, rough ice, and new ice. The PALSAR image only covered the southwestern part of the rough ice and has not been included in the figure. Along the border between the

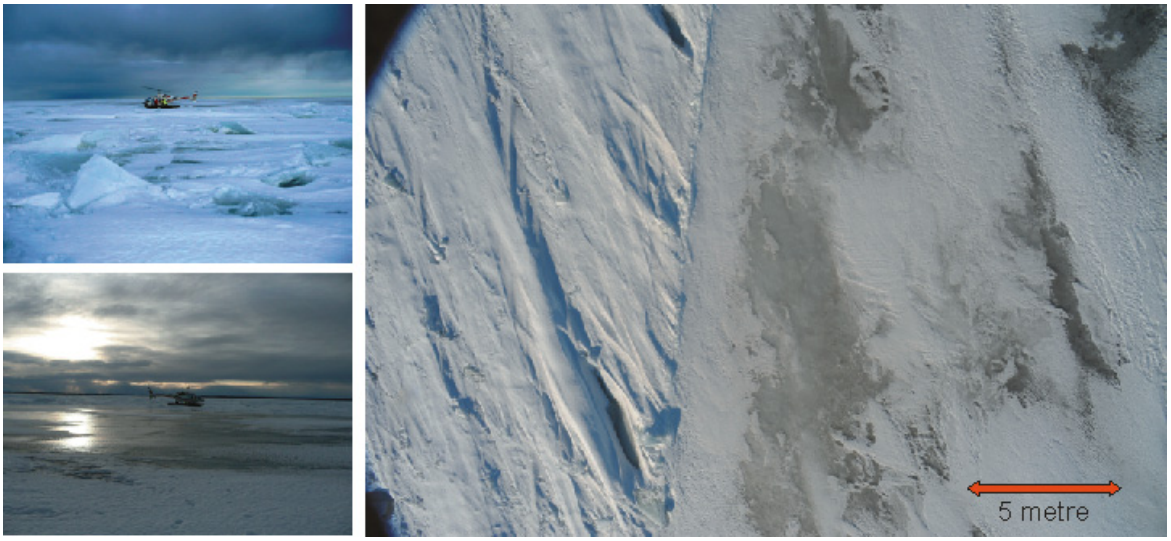

Figure 8. Photographs of the border between the rough and level fast ice taken on 21 March 2009. Upper left photo: surface structure of the rough fast ice. Lower left photo: surface of the smooth fast ice. Right photo taken from the helicopter before landing.

rough ice and open water is a narrow, bright band that consists of brash ice. A helicopter photograph of the rough ice and the brash ice is shown in **Figure 9**. Compared to the fast ice in section A, the rough ice in section B appears visually smoother. The surface is relatively homogeneous and does not consist of deformed ice, but is covered by ridges of snow. At HH polarization the rough ice has a higher backscatter than the new ice, but in the HV polarization the new ice gives higher backscatter than the rough ice. As can be seen in the plots in **Figure 10**, it is the new ice that deviates from the general trend, especially in the RADARSAT-2 image. This indicates that volume-scattering effects influence the cross-polarized signal relatively strongly. It is recognized that some C-band cross-polarized backscatter values (RADARSAT-2, 20°) are even larger than those at X-band cross-polarization (TerraSAR-X 22°), which indicates that the different penetration depths must be taken into account and that either volume characteristics change with depth or the ice–water interface affects the radar signal.

The upper left plot in **Figure 10** shows good separation between the selected ice types at HH polarization of the L-band image (ALOS PALSAR). For the C-band (RADARSAT-2 and ENVISAT ASAR) there is a slight overlap at HH polarization for the ice types level fast ice and rough ice. This overlap increases for X-band (TerraSAR-X). The plots also confirm the large backscatter variability for level fast ice in the HV polarization for ALOS PALSAR.

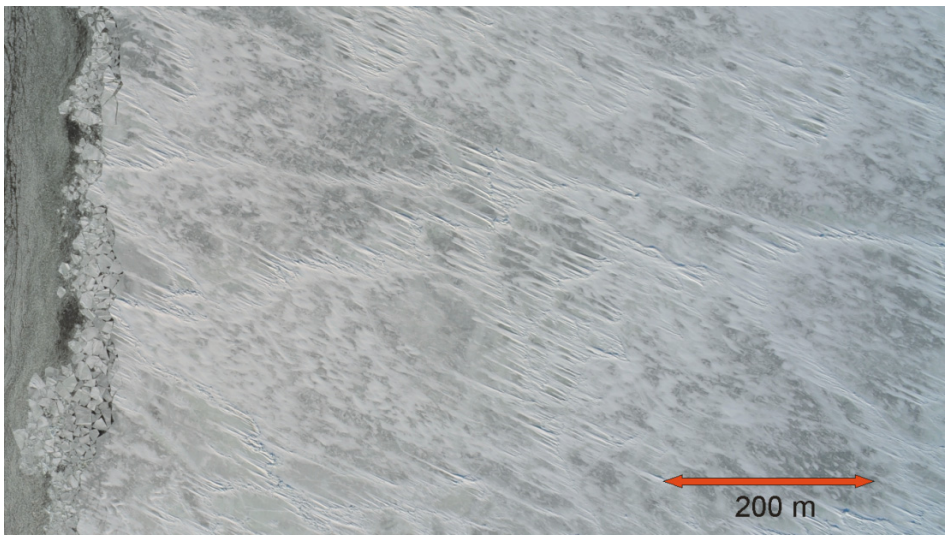

Figure 9. Helicopter photograph showing the rough ice type on 21 March 2009.

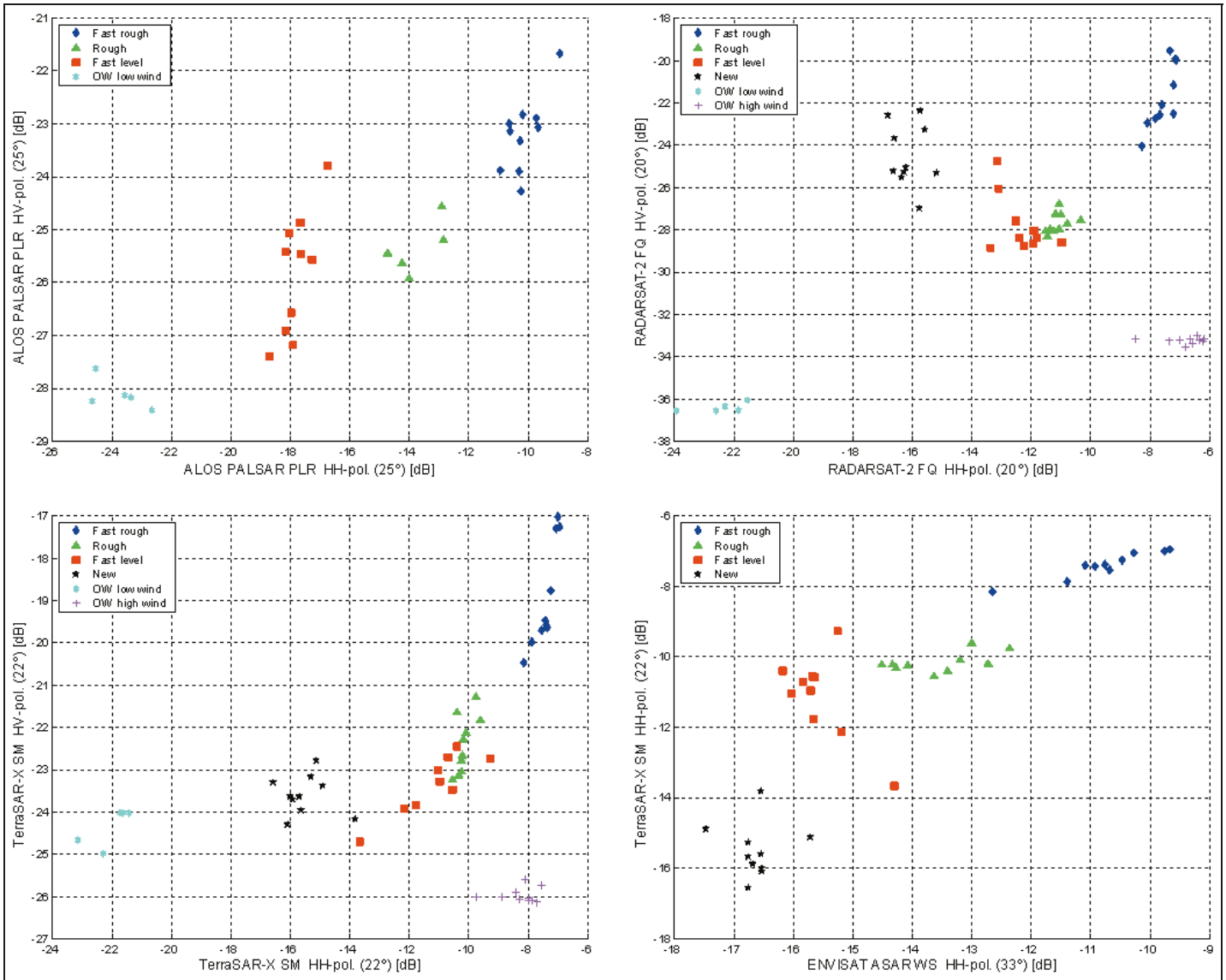

Figure 10. Backscattering coefficients of the major ice classes observed on 21 and 22 March 2009 at the test site in the Baltic Sea.

In three of the plots in **Figure 10**, backscatter signatures from open water (OW) have been included. The L-band image only contained low backscatter for open water, whereas the C- and X-band images included areas with both low and high backscatter. In the latter case the HH backscatter from open water was as high as that for the rough fast ice. The range from the lowest to the highest backscatter values for open water in HH polarization covers the whole range of values from the chosen ice types. This makes it impossible to do automatic classification of ice types based only on HH backscatter values. However, in HV polarization the RADARSAT-2 image shows a separation between open water and ice that is larger than 4 dB. For X-band there is a small overlap between open water and new and level fast ice, but combined with the HH-polarized backscatter it should be possible to distinguish between open water and ice.

Results from 23 and 24 April 2009

Based on the availability of satellite data, the best period for comparison of ScanSAR images from different satellites occurred at the end of the ice season (23 and 24 April). The area with overlapping satellite images is located in the central part of the Bothnian Bay. This region is outside the campaign area, so there are no pictures available from the helicopter and no ice observations. In **Table 1** the types of images acquired from the different satellites are shown for these dates. The pixel sizes of the analyzed images were 100 m × 100 m for ALOS PALSAR, 75 m × 75 m for Envisat ASAR, 50 m × 50 m for RADARSAT-2 SCW, 25 m × 25 m for RADARSAT-2 SCN, and 33 m × 33 m for TerraSAR-X. Ten ROIs were selected for each of the three ice types that were most common in the images. All ROIs have an area in the range between 0.33 and 0.40 km^2.

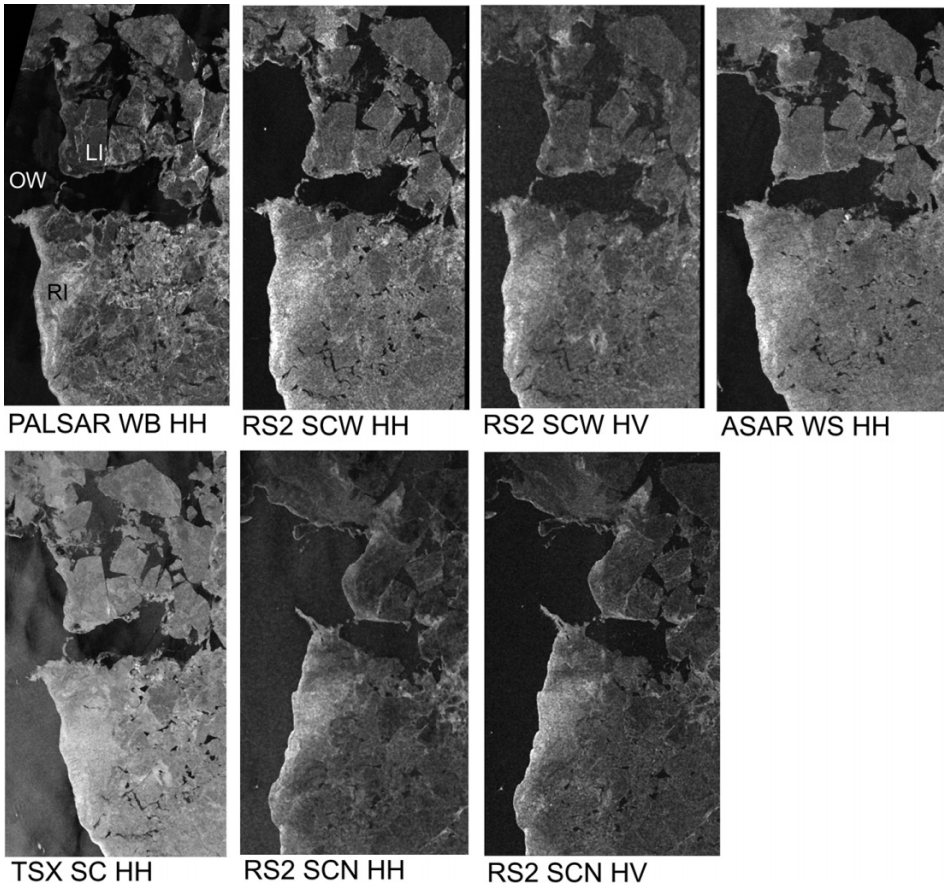

Figure 11. Sections of ScanSAR images from four different satellites. Open water (OW), rough ice (RI), and level ice (LI) are marked. All images were acquired on 23 April 2009, except the RADARSAT-2 (RS2) SCN from 24 April 2009.

In the ALOS PALSAR image the ROIs are located at incidence angles of 40.0–42.9°, which is comparable to the corresponding incidence angles in the Envisat ASAR image (range from 37.6° to 39.2°). The steepest incidence angles are found in the TerraSAR-X image, where the ROIs are located between 26.4° and 30.1°, and the RADARSAT-2 SCN image with incidence angles between 30.3° and 32.5°. The RADARSAT-2 SCW image has the highest incidence angles, which range from 47.9° to 49.2°.

Data from the Finnish meteorological station Kemi1 show that the wind speed was around 5–7 m/s on 23 April, increasing slightly the next day. The wind direction was mostly southwesterly on 21 and 22 April, shifting to the west-northwest on 23 April and then returning to the southwest on 24 April. It was sunny during this period, and the temperature was above 0 °C, with a maximum close to 5 °C. Meteorological stations along the Swedish coast recorded similar wind speeds and temperatures up to 9 °C (see **Table 1**).

A segment of the overlap area for the satellite images is shown in **Figure 11**. The contrast between ice and open water is high in all images, although in the TerraSAR-X image the wind gives relatively high backscatter over open water. In this image the contrast is in some cases higher between ice and open water *within* the pack ice, since here the wind effect is lower. In general, all images show the distribution and main structure of the ice, but details are more easily recognized in the L-band image. At the longer wavelengths, ice ridges reveal a backscattering intensity that is considerably higher than that of level ice, whereas at shorter wavelengths the small-scale roughness of the level ice raises its backscattering intensity and reduces the intensity contrast relative to that of the ridges. Longer wavelengths also give greater penetration, which make L-band images less sensitive to snow cover.

The backscatter values for the rough and level ice types are plotted in **Figure 12** for the satellite images that were available on 23 April. In addition, backscatter values have been included for fast ice outside Luleå in the northwestern part of the Bothnian Bay. The most remarkable observation from these plots is that the backscatter values for the fast ice are lower than those for level and rough ice. A possible explanation is that a larger amount of snow could have accumulated on the fast ice than on the drifting ice and, with

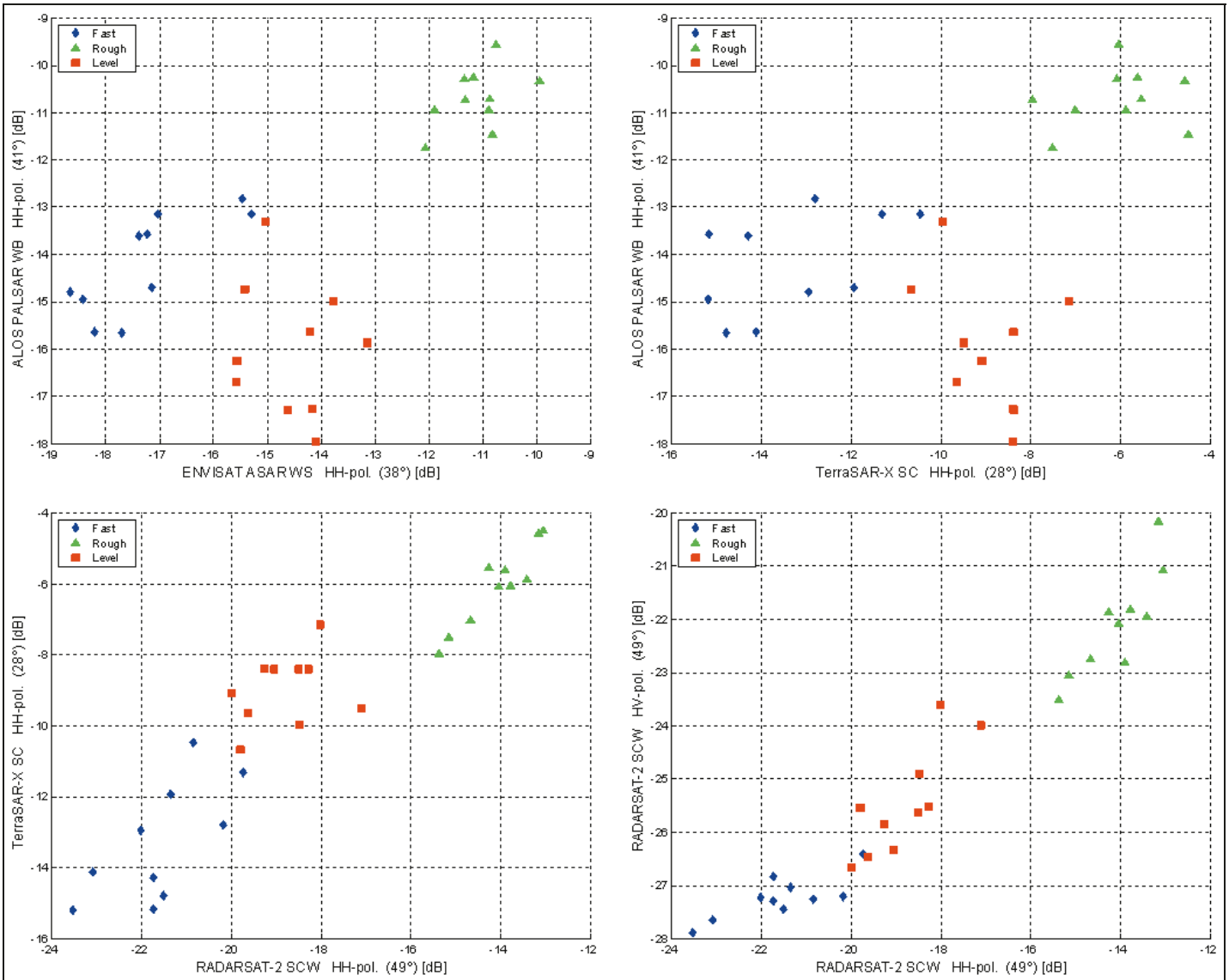

Figure 12. Backscattering coefficients of the major ice classes observed on 23 and 24 April 2009 at the test site in the Baltic Sea.

temperatures well above zero (see **Table 1**), the melting snow gives a stronger attenuation of the radar signal, leading to weaker backscatter from the ice.

Another segment, now from the eastern part of the pack ice, is presented in **Figure 13**. This area is only covered by the ALOS and Envisat images from 23 April and the RADARSAT-2 image from 24 April. In the region within the upper red ellipse, many structures such as ridges, patches of smooth ice, openings, and ship tracks are clearly visible in the ALOS PALSAR image. In the ASAR image these features are not at all as prominent except for the openings in the ice, which stand out. More structures are found in the RADARSAT-2 SCN (HH polarization) image, but it still provides far less detail than that discerned in the ALOS PALSAR image. It should be noted that the RADARSAT-2 SCN image has a higher resolution and is taken 1 day later when the southwesterly wind has caused a change in the size, shape, and number of openings in the pack ice.

In the lower, red ellipse in **Figure 13**, an area surrounded by deformed ice is distinguished in both the PALSAR and ASAR images but is less visible in the RADARSAT-2 SCN images. The PALSAR and ASAR images were obtained in the morning and evening, respectively, on 23 April. The RADARSAT-2 image was acquired in the late afternoon the following day. The temperature record from the meteorological station Kemi1 does not provide any explanation for the differences in the ASAR and RADARSAT-2 images. According to weather radar, however, there were some minor areas of precipitation in the region a couple of hours before the RADARSAT-2 image was obtained. It is possible that this image is affected by wet snow that masks some of the structural differences in the

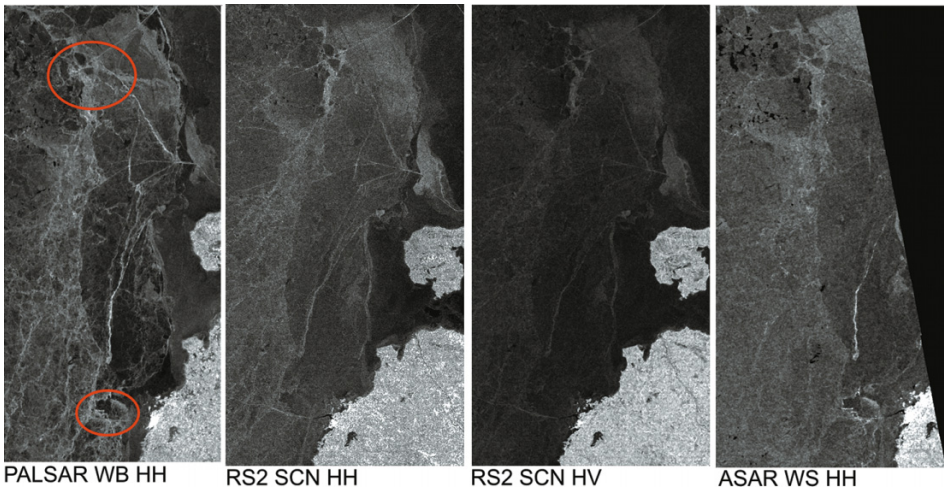

Figure 13. Sections from four ScanSAR images. Areas discussed in the text are marked with red ellipses.

ice. At L-band, the penetration through the snow is higher, so the signal from the ice is less affected.

Discussion and conclusions

The aim of this paper was to identify advantages and disadvantages of different spaceborne SAR systems and imaging modes for operational sea-ice monitoring in the Baltic Sea, with a special focus on different frequencies, polarizations, and spatial resolutions.

In general, all three new satellite radars (ALOS, TerraSAR-X, and RADARSAT-2) deliver data that provide possibilities for ice classification similar to those of the currently used C-band data with HH polarization, though with distinct differences in details. One problem for copolarized (HH or VV) data at C-band is the highly variable backscatter levels from open water, which for certain wind conditions make the discrimination between open water and sea ice difficult. This problem remains for both L-band and X-band but can be reduced by adding cross-polarized data, which do not show the same dependency on wind speed and wind direction. The combination of copolarized and cross-polarized data could therefore potentially lead to improved algorithms for retrieval of ice concentration. Ice ridges are also easier to identify in cross-polarized data, but for classification purposes it has to be considered that the signal-to-noise ratio is rather low in particular for new ice. At L-band like polarization, ice ridges and ice structures are also easier to identify. The information content of X- and C-band images is largely equivalent, whereas L-band data provide complementary information because they are considerably less affected by microscale ice structures. The longer wavelength also seems to give a lower sensitivity to wet snow.

From an operational point of view, the swath width of TerraSAR-X is too small to give the required spatial coverage, and the current observational plan for ALOS will not provide an update frequency that is high enough to compete with Envisat or RADARSAT-2 as the operational workhorses for sea-ice monitoring, but the study has shown that ALOS can be used to fill in gaps in the temporal or spatial coverage. TerraSAR-X might find its niche for high-resolution monitoring of geographically limited areas like lakes, rivers, harbours, or shipping routes with high traffic. Many of the findings in this study should also be applicable for most of the near-future spaceborne SAR systems, as L-, C-, and X-bands will continue to be the main frequency bands for SAR.

Acknowledgments

This work was funded by the Swedish National Space Board (dnr 158/06), the Swedish Meteorological and Hydrological Institute, and the Swedish Maritime Administration. Data from ALOS and Envisat were provided by the European Space Agency within the framework of the ALOS Data European node category-1 proposal titled Improved sea-ice monitoring for the Baltic Sea (AOALO.3562). Data from TerraSAR-X were provided by the German Aerospace Center (DLR) under the agreement for proposal OCE0089, and data from RADARSAT-2 were granted within the Canadian program for Science and Operational Applications Research for RADARSAT-2 (SOAR), project number 3924. The Umeå Marine Science Centre in Norrbyn and Lapplandsflyg AB in Umeå are acknowledged for logistical support during the field campaigns.

References

Askne, J., Leppäranta, M., and Thompson, T. 1992. The Bothnian experiment in preparation of ERS-1, 1988 (BEPERS-88), an overview. *International Journal of Remote Sensing*, Vol. 13, No. 13, pp. 2377–2399.

Carlström, A. 1995. *Modelling microwave backscattering from sea ice for synthetic aperture radar applications*. School of Electrical and Computer Engineering, Chalmers University of Technology, Göteborg, Sweden. Technical Report 271.

Dammert, P., Ulander, L.M.H., and Larsson, B. 1994. ERS-1 SAR signatures of sea ice and leads. In *Baltic experiment for ERS-1 (BEERS)*. Edited by L.M.H. Ulander. Winter Navigation Research Board, National Maritime Administration, Norrköping, Sweden. Research Report 51, pp. 71–98.

Dierking, W. 1999. Quantitative roughness characterization of geological surfaces and implications for radar signature analysis. *IEEE Transactions on Geoscience and Remote Sensing*, Vol. 37, No. 5, pp. 2397–2412.

Dierking, W., and Askne, J. 1998. Polarimetric L- and C-band signatures of Baltic Sea ice observed during EMAC-95. In *Future trends in remote sensing*. Edited by P. Gudmandsen. A.A. Balkema, Rotterdam, The Netherlands. pp. 329–336.

Dierking, W., and Busche, T. 2006. Sea ice monitoring by L-band SAR: An assessment based on literature and comparisons of JERS-1 and ERS-1 imagery. *IEEE Transactions on Geoscience and Remote Sensing*, Vol. 44, No. 2, pp. 957–970.

Dierking, W., and Dall, J. 2007. Sea ice deformation state from synthetic aperture radar imagery — part 1: comparison of C- and L-band and different polarizations. *IEEE Transactions on Geoscience and Remote Sensing*, Vol. 45, No. 11, pp. 3610–3622. doi:10.1109/TGRS.2007.903711.

Dierking, W., Askne, J., and Pettersson, M.I. 1997. Baltic Sea ice observations during EMAC-95 using multifrequency scatterometry and EMISAR data. In *EMAC 94/95 Final Results, Workshop Proceedings*. European Space Agency (ESA) Publications Division, ESTEC, Noordwijk, The Netherlands. ESA WPP-136, pp. 171–177.

Dierking, W., Pettersson, M.I., and Askne, J. 1999. Multifrequency scatterometer measurements of Baltic Sea ice during EMAC-95. *International Journal of Remote Sensing*, Vol. 20, No. 2, pp. 349–372.

Eriksson, L.E.B., Borenäs, K., Dierking, W., Pemberton, P., Griph, S., and Lindh, H. 2007. Improved sea-ice monitoring for the Baltic Sea — Project overview and first results. In *Proceedings of the 1st Joint PI Symposium of ALOS Data Nodes for ALOS Science Program in Kyoto*, 19–23 November 2007, Kyoto, Japan. Japan Aerospace Agency (JAXA), Tokyo. JAXA-SP-07-012.

Eriksson, L.E.B., Borenäs, K., Dierking, W., Berg, A., Pemberton, P., Lindh, H., Karlson, B., and Santoro, M. 2010. Improved sea-ice monitoring for the Baltic Sea — Project summary. In *Proceedings of the 3rd International Workshop on Advances in SAR Oceanography from Envisat, ERS and ESA Third Party Missions SeaSAR 2010*, 25–29 January, 2010, Frascati, Italy. European Space Agency (ESA) Publications Division, ESTEC, Noordwijk, The Netherlands. ESA SP-679.

Fransson, L., Håkansson, B., Omstedt, A., and Stehn, L. 1990. *Sea ice properties studied from the icebreaker Tor during BEPERS-88*. Swedish Meteorological and Hydrological Institute (SMHI), Norrköping, Sweden. SMHI Reports of Oceanography No. 10. 20 pp.

Gogineni, S.P., Moore, R.K., Grenfell, T.C., Barber, D.G., Digby, S., and Drinkwater, M. 1992. The effect of freeze-up and melt processes on microwave signatures. In *Microwave remote sensing of sea ice*. Edited by F.D. Carsey. American Geophysical Union (AGU), Washington, D.C. Geophysical Monograph 68, pp. 329–341.

Grafström, T., and Kilgren, D. 2008. *A summary of the ice season and icebreaking activities 2007/2008*. Swedish Marine Administration and the Swedish Meteorological and Hydrological Institute (SWHI), Norrköping, Sweden.

Granskog, M., Kaartokallio, H., Kuosa, H., Thomas, D.N., and Vainio, J. 2006. Sea ice in the Baltic Sea — A review. *Estuarine, Coastal and Shelf Science*, Vol. 70, No. 1–2, pp. 145–160.

Hallikainen, M. 1992. Microwave remote sensing of low-salinity sea ice. In *Microwave remote sensing of sea ice*. Edited by F. Carsey. American Geophysical Union (AGU), Washington, D.C. Geophysical Monograph 68, pp. 361–373.

Hyppä, J., and Hallikainen, M. 1992. Classification of low-salinity sea ice types by ranging scatterometer. *International Journal of Remote Sensing*, Vol. 13, No. 13, pp. 2399–2413.

Leppäranta, M., and Manninen, T. 1988. *The brine and gas content of sea ice with attention to low salinities and high temperatures*. Finnish Institute of Marine Research, Helsinki, Finland. Internal Report 88-2.

Leppäranta, M., Kuttinen, R., and Askne, J. 1992. BEPERS pilot study: an experiment with X-band synthetic aperture radar over Baltic Sea ice. *Journal of Glaciology*, Vol. 38, No. 128, pp. 23–35.

Mäkynen, M. 2007. *Investigation of the microwave signatures of the Baltic Sea ice*. Laboratory of Space Technology Publications, Helsinki University of Technology, Espoo, Finland. Report 59.

Mäkynen, M., and Hallikainen, M. 2004. Investigations of C- and X-band backscattering signatures of Baltic Sea ice. *International Journal of Remote Sensing*, Vol. 25, No. 11, pp. 2061–2086.

Matsuoka, T., Uratsuka, S., Satake, M., Kobayashi, T., Nadai, A., Umehara, T., Maeno, H., Wakabayashi, H., Nakamura, K., and Nishio, F. 2001. CRL/NASDA airborne SAR (Pi-SAR) observations of sea ice in the Sea of Okhotsk. *Annals of Glaciology*, Vol. 33, pp. 115–119.

Matsuoka, T., Uratsuka, S., Satake, M., Nadai, A., Umehara, T., Maeno, H., Wakabayashi, H., Nishio, F., and Fukamachi, Y. 2002. Deriving sea-ice thickness and ice types in the Sea of Okhotsk using dual-frequency airborne SAR (Pi-SAR) data. *Annals of Glaciology*, Vol. 34, pp. 429–434.

Melling, H. 1998. Detection of features in first-year pack ice by synthetic aperture radar (SAR). *International Journal of Remote Sensing*, Vol. 19, No. 6, pp. 1223–1249.

Nghiem, S.V., Borgeaud, M., Kong, J.A., and Shin, R.T. 1990. Polarimetric remote sensing of geophysical media with layer random medium model. In *Progress in electromagnetic research. Volume 3: polarimetric remote sensing*. Edited by J.A. Kong. Elsevier, New York. Chapt. 1, pp. 1–73.

Nghiem, S.V., Kwok, R., Yueh, S.H., Kong, J.A., Hsu, C.C., Tassoudji, M.A., and Shin, R.T. 1995. Polarimetric scattering from layered media with multiple species of scatterers. *Radio Science*, Vol. 30, No. 4, pp. 835–852.

Onstott, R.G. 1992. SAR and scatterometer signatures of sea ice. In *Microwave remote sensing of sea ice*. Edited by F. Carsey. American Geophysical Union (AGU), Washington, D.C. Geophysical Monograph 68, pp. 73–104.

Pearson, D., Livingstone, C.E., Hawkins, R.K., Gray, A.L., Arsenault, L.D., Wilkenson, T.L., and Okamoto, K. 1980. Radar detection of sea-ice ridges and icebergs in frozen oceans at incidence angles from 0° to 90°. In *Proceedings of the 6th Canadian Symposium on Remote Sensing*, 21–23 May 1980, Halifax, N.S. Canadian Aeronautics and Space Administration (CASI), Ottawa, Ont. pp. 231–237.

Seinä, A., and Palosuo, E. 1996. The classification of the maximum annual extent of ice cover in the Baltic Sea 1720–1995. *MERI Report Series of the Finnish Institute of Marine Research*, Vol. 27, pp. 79–91.

Similä, M., Heiler, I., Mäkynen, M., and Hallikainen, M. 1998. Discrimination properties of polarimetric SAR data over the Baltic Sea ice. In *Proceedings of Earth Surface Remote Sensing II*, 21 September 1998, Barcelona, Spain. Edited by G. Cecchi and E. Zilioli. The International Society for Optical Engineering, Bellingham, Wash. Proceedings of SPIE Volume 3496, pp. 150–165.

Skriver, H., Quegan, S., LeToan, T., Dierking, W., Gudmandsen, P., Papathanassiou, K.P., and Moreira, A. 2004. *Application of synthetic aperture radar polarimetry: final report (POLSAR/FR)*. European Space Agency (EAS), Publications Division, ESTEC, Noordwijk, The Netherlands. ESA Study Contract Report 15600/01/I-LG, pp. 193–302.

Thomsen, B.B. 2001. *Polarimetric signatures of thin sea ice*. Ph.D. thesis, Oersted DTU, Department of Electromagnetic Systems, Technical University of Denmark, Lyngby, Denmark. Report LD143.

Ulander, L.M.H. 1991. *Radar remote sensing of sea ice*. School of Electrical and Computer Engineering, Chalmers University of Technology, Göteborg, Sweden. Technical Report 212.

Ulander, L.M.H., Johansson, R., and Askne, J. 1992. C-band radar backscatter of Baltic Sea ice: theoretical predictions compared with calibrated SAR measurements. *International Journal of Remote Sensing*, Vol. 13, No. 13, pp. 2447–2468.

Vancoppenolle, M., Fichefet, T., and Goosse, H. 2009. Simulating the mass balance and salinity of Arctic and Antarctic sea ice. 2. Importance of sea ice salinity variations. *Ocean Modelling*, Vol. 27, No. 1–2, pp. 54–69.

Wegmüller, U. 1999. Automated terrain corrected SAR geocoding. In *IGARSS'99, Proceedings of the International Geoscience and Remote Sensing Symposium*, 28 June – 2 July 1999, Hamburg, Germany. Edited by T.I. Stein. IEEE Publications, Piscataway, N.J. pp. 1712–1714.